Accepted Manuscript

Recent development of transient electronics

Huanyu Cheng, Vikas Vepachedu

PII: S2095-0349(15)00110-5
DOI: http://dx.doi.org/10.1016/j.taml.2015.11.012
Reference: TAML 62

To appear in: *Theoretical and Applied Mechanics Letters*

Received date: 10 October 2015
Accepted date: 26 November 2015

Please cite this article as: H. Cheng, V. Vepachedu, Recent development of transient electronics, *Theoretical and Applied Mechanics Letters* (2016), http://dx.doi.org/10.1016/j.taml.2015.11.012

***Highlights (for review)**

This review paper on transient electronics includes the following highlights:

- A number of inorganic materials and their method of application were studied.
- Models of reactive diffusion were presented to predict the dissolution behavior.
- Various encapsulation approaches were explored as a way to extend the lifetime.
- The transient ECG sensor was configured in a stretchable layout.

***Manuscript**

Recent Development of Transient Electronics

Huanyu Cheng[1*], Vikas Vepachedu[1]

[1] *Department of Engineering Science and Mechanics, Materials Research Institute, The Pennsylvania State University, University Park, Pennsylvania 16802, USA*

[*]To whom all correspondence should be addressed: huanyu.cheng@psu.edu

ABSTRACT: Transient electronics are an emerging class of electronics with unique characteristic to completely dissolve within a programmed period of time. Since no harmful byproducts are released, these electronics can be used in the human body as a diagnostic tool, for instance, or they can be used as environmentally friendly alternatives to existing electronics which disintegrate when exposed to water. Thus, the most crucial aspect of transient electronics is their ability to disintegrate in a practical manner and a review of the literature on this topic is essential for understanding the current capabilities of transient electronics and areas of future research. In the past, only partial dissolution of transient electronics was possible, however, total dissolution has been achieved with a recent discovery that silicon nanomembrane undergoes hydrolysis. The use of single- and multi-layered structures has also been explored as a way to extend the lifetime of the electronics. Analytical models have been developed to study the dissolution of various functional materials as well as the devices constructed from this set of functional materials and these models prove to be useful in the design of the transient electronics.

KEY WORDS: Transient electronics, model of reactive diffusion, encapsulation strategy, multi-layer structures

Introduction

While the development of modern electronics has typically been concerned with durable devices that function stably over time, the advent of transient electronics takes an opposite approach; the destruction of the said devices is designed to provide unique opportunities. Upon exposure to water, transient electronics disintegrate at a predictable rate while releasing biologically and/or environmentally benign end products (Hwang et al., 2012; Hwang et al., 2014b). This ability opens a wide range of applications from bio-degradable electronics to diagnostic/therapeutic implants (Darouiche, 2004; Tao et al., 2014). One can use an electronic component, for instance, as a temporary implant in a patient and allow it to safely dissolve on its own without the need for a second surgery (Dagdeviren et al., 2013; Hwang et al., 2012). Ultimately, transient electronics can solve the problem of disposing electronics in a safe and convenient manner (Hernandez et al., 2014; Lee et al., 2015; Park et al., 2015).

The defining quality of transient electronics is their ability to dissolve into non-toxic products upon exposure to water and, naturally, dissolution accounts for a significant amount of research in this field (Huang et al., 2014; Hwang et al., 2012; Hwang et al., 2015b; Hwang et al., 2014b; Kang et al., 2014; Li et al., 2013). Early research on this topic resulted in achieving the partial dissolution of components through the use of organic materials as substrates (Bettinger and Bao, 2010; Irimia-Vladu et al., 2010). For instance, organic thin-film transistors have been developed using cotton-made paper (Eder et al., 2004) as substrate and silk was also shown to be useful as a soluble substrate for implants in the body (Kim et al., 2009). However, this type of research was limited to the substrate and the electronic devices remained insoluble.

More recently however, electronics which are completely soluble have been developed. This relies on a recent, important discovery that semiconductor grade monocrystalline silicon can undergo dissolution in bio-fluids or even water at physiological conditions with a programmed lifetime relevant to applications in biomedicine (Hwang et al., 2012). As the reaction rate of silicon hydrolysis to form silicic acid ($Si(OH)_4$) is exceptionally small, silicon devices were fabricated in extremely thin forms. A nanomembrane of silicon with lateral dimensions similar to conventional circuits but with a thickness of 70 nm has been shown to dissolve in ~10 days (Hwang et al., 2012). Via similar chemistry, thin silicon dioxide (SiO_2) was selected as a gate dielectric. Taken together with the other dissolvable, inorganic materials such as magnesium

(Mg) and magnesium oxide (MgO) for conductors and the interlayer dielectric, respectively, due to their spontaneous reaction with water to form biologically benign $Mg(OH)_2$, silicon nanomembranes provide a basic means for the construction of a transient, electronic device. As a proof-of-concept, Figure 1a and b present a schematic demonstration platform which utilizes silicon nanomembranes (Si NMs) for the semiconductors, magnesium for the conductors, magnesium oxide and silicon dioxide for the dielectrics, and silk for the substrate and packaging materials. The collectively configured devices dissolve and disintegrate when immersed in deionized (DI) water (Figure 1c).

Surface reactions typically dominate the dissolution behavior for sufficiently large reaction constants. The porosity of the materials (e.g. Mg, MgO, and SiO_2) however, was found to be influential as it allows for the diffusion of water through the material, thereby increasing the dissolution rate through an increase in the effective surface area (Li et al., 2013). In studying the dissolution of transient electronics, the factors to consider include physical and chemical properties of materials, and certain ambient factors of an aqueous environment. Given the research of these factors and others, analytical models have been developed to solidify the understanding of the dissolution behaviors in transient electronics (Hwang et al., 2012; Kang et al., 2014; Li et al., 2013). Such models can be of great assistance in the design of transient electronics. This review will first provide a comprehensive discussion on the hydrolysis of semiconducting materials with a focus on silicon nanomembranes, followed by the model of reactive diffusion to account for the dissolution behavior of porous materials. When combined with ideas from soft, tissue-like electronic devices, the class of transient electronics provides a viable means to monitor health or deliver care in a minimally obtrusive way.

Hydrolysis of Semiconducting Materials

To establish a realistic set of functional materials, knowledge regarding the chemical kinetics of each material is critical, especially that of the hydrolysis of semiconducting materials. At physiological pH levels and temperatures, the dissolution rates of semiconducting materials (e.g. silicon, silicon-germanium, and germanium) are remarkably small (Kang et al., 2015). Therefore, in order to minimize the amount of semiconducting materials which must be dissolved, the nanomembrane structure is critical. Dissolution of monocrystalline silicon

nanomembranes in phosphate buffered saline (PBS with pH=7.4) at biologically pertinent temperatures (e.g., 37^{o}) forms either an intermediate oxidation product SiO_2 or silicic acid $Si(OH)_4$ through the equilibrium: $Si+4H_2O <-> Si(OH)_4+2H_2$ (Rimstidt and Barnes, 1980; Seidel et al., 1990b). The rate depends on the crystal structure, morphology, and doping concentration of silicon (Hwang et al., 2014a; Seidel et al., 1990a), as well as the temperature and composition of solutions (Hwang et al., 2014b; Seidel et al., 1990b).

Systematic characterization of the dissolution kinetics for silicon used various bio-fluids at multiple pH levels and temperatures. Patterned Si NMs (3 m × 3 m × 70 nm) were first created on a layer of thermal oxide on a silicon wafer, followed by immersion in aqueous buffer solutions (50 mL, in a petri dish with diameter of 7 cm). The dissolution rate of thermal oxide is negligible in comparison to that of silicon. Thicknesses of Si NMs were measured at a specific time (e.g., every other day) after which the sample was placed into a fresh buffer solution. There was no significant change in the dissolution rate for a variety of time intervals (e.g. for every 1, 2, 4, 7 days), indicating accurate measurement in the dissolution rate. Studies of SiGe and Ge were given in a similar setup (Kang et al., 2015). Figure 2a presents atomic force microscope topographical images of a Si NM with an initial thickness of 70 nm collected at various stages of hydrolysis, demonstrating its transient behavior in bio-fluids (PBS with pH of 7.4; 37 °C).

Given the dense arrangement of the silicon atoms in crystal structures, the hydrolysis of monocrystalline silicon nanomembranes is limited to the surface and the kinetics can be described by a surface reaction with a constant dissolution rate (Hwang et al., 2012; Hwang et al., 2014b). With the assumption that no solution molecules diffuse into the silicon, this model yields a linear relationship between the measured thickness and the time, where the slopes represent the dissolution rates. A previously established empirical formula (Seidel et al., 1990b) suggests that an increase in the hydroxide ion concentration $[OH^{-}]$ results in an accelerated dissolution rate in high pH solutions of KOH. As shown in Figure 2b, this formula can reproduce the experimental trends for solutions at the physiological pH levels if a different power law exponent is used for $[OH^{-}]$ (Hwang et al., 2014b).

In conjunction with the pH levels, the type and concentration of ions also have appreciable effects on the dissolution process. Experimental data show the dissolution rate of silicon in bovine serum (≈protein 40 g L^{-1}, ≈0.12 M sodium chlorides, pH 7.4 at 37 °C) is 20 times higher than that in the phosphate buffered saline solution at comparable pH (≈0.14 M chlorides and 0.01

M phosphates, pH 7.4 at 37 °C). In an effort to examine the underlying aspects of concentration of anions found in the biological systems such as chlorides (Cl^-) and phosphates (HPO_4^{2-}), studies on dissolution of Si NMs as a function of ion concentration (chlorides and phosphates, 0.05M-1M) were performed at a pH level fixed at 7.5 (Yin et al., 2015). Experimental measurements indicate a power law dependence of dissolution rates on $\left[Cl^-\right]$ and $\left[HPO_4^{2-}\right]$, as for [OH^-] in high pH solutions of KOH. A layer by layer dissolution of Si NMs at the surface is an effect of nucleophilic attack by OH^- of silicon surface bonds, which weakens the interior bonds of surface silicon. The other anions can also promote the dissolution of Si NMs as they act as nucleophiles. Atomic level simulations show elongated interior bonds of surface silicon after adsorption of OH^-, Cl^-, and HPO_4^{2-}, suggesting a decrease in their strength. A schematic representation of the ion adsorption process on the silicon surface is shown in Figure 2c. With the capability to interact with silicon surface in a manner similar to OH^-, nucleophilic anions such as Cl^- and HPO_4^{2-} assist the dissolution of Si NMs (Yin et al., 2015).

In order to construct functional devices, the dissolution of doped silicon with different types and concentrations is of importance as well. Consistent with the prior study of silicon dissolution at comparatively high pH levels and temperatures (Seidel et al., 1990a), the measurement of Si NMs doped with phosphorus (P) or boron (B) at different concentrations indicate a significant reduction in dissolution rates when dopant concentrations surpass a certain level (e.g. 10^{20} cm^{-3}). As described by an empirical expression $R_{dissolution} = R_i \Big/ \left[1+\left(C/C_0\right)^4\right]$, the dissolution rate remains constant (R_i) until a critical dopant concentration (C_0) is reached and then the rate decreases sharply. In the empirical expression, R_i and C_0 depend on temperature following an Arrhenius law with different activation energies. This empirical expression also captures the dissolution behavior of doped silicon in physiologically relevant conditions (Hwang et al., 2014a).

Model of Reactive Diffusion for Transient Materials

In addition to surface reactions, the diffusion in the porous materials cannot be ignored and the reaction between the diffused molecules and surrounding porous materials also needs to be considered. A model of reactive diffusion was proposed to analytically study the dissolution

process of porous materials (Danckwerts, 1950). The model considers the diffusion of water and hydroxide ions into porous materials, which effectively increases the reactive surface. Here the key parameters are the diffusivity D of water in the porous material and the reaction constant k between water and the material. Because the initial thickness h_0 is much smaller than both the width and length of the sample in the experiment, the one-dimensional model (1D) can adequately capture the dissolution behaviors. With y=0 at the bottom of the material layer (Figure 4a), the water concentration $w(y, t)$ at location y and time t satisfies the reactive diffusion equation (Danckwerts, 1950)

$$D\frac{\partial^2 w}{\partial y^2} - kw = \frac{\partial w}{\partial t},\ 0 \le y \le h_0. \tag{1}$$

This equation reduces to the standard diffusion equation if the reaction constant k is negligible. The boundary conditions of Equation (1) include a constant water concentration at the water/porous material interface $w|_{y=h_0} = w_0$ and a zero water flux at the porous material/substrate interface $\partial w/\partial y|_{y=0} = 0$. The initial condition is zero water concentration $w|_{t=0} = 0\ (0 \le y < h_0)$. In order to transform the inhomogeneous boundary condition $w|_{y=h_0} = w_0$ to a homogenous one, a new variable $\theta = w - w_0$ is introduced (Li et al., 2013), which results in an updated equation

$$D\frac{\partial^2 \theta}{\partial y^2} - k\theta - \frac{\partial \theta}{\partial t} = kw_0,\ 0 \le y \le h_0. \tag{2}$$

The boundary conditions and the initial condition become $\theta|_{y=h_0} = 0$, $\partial\theta/\partial y|_{y=0} = 0$, and $\theta|_{t=0} = -w_0\ (0 \le y < h_0)$, respectively. Equation (2) is inhomogeneous, but the general solution can be represented by a sum of a homogeneous solution θ_h and a particular solution θ_p. The homogenous solution θ_h satisfies the homogeneous equation $D\partial^2\theta_h/\partial y^2 - k\theta_h - \partial\theta_h/\partial t = 0$ with homogeneous boundary conditions $\theta_h|_{y=h_0} = 0$ and $\partial\theta_h/\partial y|_{y=0} = 0$. Expressed in the form of $\theta_h = Y(y)T(t)$, θ_h can be solved by the method of separation of variables. The homogeneous equation leads to $DY''/Y - k = T'/T = -\lambda$, where λ is the eigenvalue to be determined from the boundary condition. The functions $T(t)$ and $Y(y)$ are then expressed as $T = e^{-\lambda t}$ and

$Y = A\sin\left[\sqrt{(\lambda-k)/D}\,y\right] + B\cos\left[\sqrt{(\lambda-k)/D}\,y\right]$, where A and B are constants to be determined from initial and boundary conditions. With $Y|_{y=h_0} = 0$ and $Y'|_{y=0} = 0$ obtained from the homogeneous boundary conditions, A is solved to be $A = 0$ and the trigonometric equation $\cos\left[\sqrt{(\lambda-k)/D}\,h_0\right] = 0$ leads to the solution for eigenvalues $\lambda_n = \left[(2n-1)\pi/(2h_0)\right]^2 D + k \quad (n = 1, 2, 3, \ )$, which in turn gives the homogeneous solution

$$\theta_h = \sum_{n=1}^{\infty}\left\{B_n e^{-\left[\left(\frac{2n-1}{2h_0}\pi\right)^2 D + k\right]t}\cos\left(\frac{2n-1}{2h_0}\pi y\right)\right\}, \tag{3}$$

with constants B_n to be determined from the initial condition. The particular solution θ_p needs to satisfy the inhomogeneous equation and homogeneous boundary conditions. A suitable choice is $\theta_p = w_0\left[\cosh\left(\sqrt{k/D}\,y\right)/\cosh\left(\sqrt{k/D}\,h_0\right) - 1\right]$. The substitution of the general solution $\theta = \theta_h + \theta_p$ in the initial condition leads to $B_n = 4(-1)^n(2n-1)\pi D w_0/\left[4kh_0^2 + (2n-1)^2\pi^2 D\right]$, from which the solution of Equation (1) is obtained as

$$w(y,t) = w_0\left\{\frac{\cosh\left(\sqrt{\frac{kh_0^2}{D}}\frac{y}{h_0}\right)}{\cosh\sqrt{\frac{kh_0^2}{D}}} + 2\sum_{n=1}^{\infty}\frac{(-1)^n\left(n-\frac{1}{2}\right)\pi}{\frac{kh_0^2}{D}+\left(n-\frac{1}{2}\right)^2\pi^2}e^{-\left[\frac{kh_0^2}{D}+\left(n-\frac{1}{2}\right)^2\pi^2\right]\frac{Dt}{h_0^2}}\cos\left[\left(n-\frac{1}{2}\right)\pi\frac{y}{h_0}\right]\right\}. \tag{4}$$

The solution given above indicates a clear scaling law $w/w_0 = \overline{w}\left(y/h_0, Dt/h_0^2, kh_0^2/D\right)$ that the normalized water concentration w/w_0 depends on normalized position y/h_0, normalized time Dt/h_0^2, and a single non-dimensional parameter kh_0^2/D that scales with the ratio of reaction constant k to diffusivity D. Experiment measurement of Mg with an initial thickness of 300 nm shows D=6.0×10^{-12} cm^2/s and k=1.2×10^{-3} s^{-1} which is within the range of reaction constants reported by Taub et al. (Taub et al., 2002). Figure 3a presents the distribution of water concentration for the normalized time Dt/h_0^2 =0.1, 0.2, 0.4, 0.8, 2 and ∞, where $Dt/h_0^2 = \infty$ corresponds to

the steady-state limit of the water concentration in the Mg layer $w(y, t\to\infty) = w_0 \cosh\left(\sqrt{kh_0^2/D}\, y/h_0\right)\Big/\cosh\sqrt{kh_0^2/D}$.

Realizing the definition of the reaction constant, the mass of water reacted at a given location (per unit volume) is kw. When q water molecules react with one atom of the porous material, the mass of the dissolved porous material (per unit volume) at this location is $kwM/\left(qM_{H_2O}\right)$, where M and $M_{\mathrm{H_2O}} = 18\,\mathrm{g\cdot mol^{-1}}$ are the molar masses of porous material and water, respectively. Integration of $kwM/\left(qM_{H_2O}\right)$ over both the thickness y and time t yields the total dissolved mass of porous material, which in turn gives a scaling law of the remaining thickness h normalized by its initial thickness h_0, before complete physical disappearance, as

$$\frac{h}{h_0} = 1 - \frac{w_0 M}{q\rho M_{H_2O}}\frac{kh_0^2}{D}\left\{\frac{Dt}{h_0^2}\cdot\frac{\tanh\sqrt{\frac{kh_0^2}{D}}}{\sqrt{\frac{kh_0^2}{D}}} - 2\sum_{n=1}^{\infty}\frac{1-e^{-\left[\frac{kh_0^2}{D}+\left(n-\frac{1}{2}\right)^2\pi^2\right]\frac{Dt}{h_0^2}}}{\left[\frac{kh_0^2}{D}+\left(n-\frac{1}{2}\right)^2\pi^2\right]^2}\right\}, \tag{5}$$

where ρ is the mass density of the porous material. For parameters k and D relevant to applications of transient electronics in biomedicine, the summation on the right hand side of Equation (5) is negligible in comparison with the other term, leading to a simple and approximately linear expression for the thickness as $h/h_0 \approx 1 - t/t_c$, where $t_c = \left(h_0/\sqrt{kD}\right)\left[q\rho M_{H_2O}/(w_0 M)\right]\left(\tanh\sqrt{kh_0^2/D}\right)^{-1}$ is the critical time of complete physical disappearance for the transient material. The rate of dissolution $v_{\mathrm{dissolution}}$, also known as the electrical dissolution rate used for conductors (Yin et al., 2014), can be determined from the linear approximation of the thickness as $v_{dissolution} = -dh/dt \approx h_0/t_c = \sqrt{kD}\, w_0 M/\left(q\rho M_{H_2O}\right)\tanh\sqrt{kh_0^2/D}$. The rate of dissolution is 0.044 nm/s, 0.13 nm/s, and 0.20 nm/s for 100 nm-, 300 nm- and 500 nm-thick Mg layers, respectively. These quantities have the same order of magnitude as rates of dissolution reported in the prior experiments (Inoue et al., 2002; Ng et al., 2010).

The chemical reaction of Mg in phosphate buffered saline follows Mg + 2 H_2O → $Mg(OH)_2$ + H_2. Thus, two water molecules react with one Mg atom (i.e., q=2). Because water molecules are the dominant molecule in phosphate buffered saline or the other bio-fluids, the wa-

ter concentration is approximately W_0=1 g·cm^{-3}. The critical time t_c to dissolve Mg (molar mass M=24 g·mol^{-1}, mass density ρ=1.738 g·cm^{-3}, and initial thickness h_0=300 nm) is calculated as 38 minutes, which agrees reasonably well with the measurement of 40 min in the experiment. Via a similar chemistry, one silicon oxide atom reacts with two water molecules by SiO_2 + 2 H_2O → $Si(OH)_4$. Because the reaction between SiO_2 and water is much slower than between Mg and water (minutes to dissolve Mg versus days to dissolve SiO_2), the reaction constant between water and SiO_2 (~10^{-6} s^{-1}) is much smaller than that between water and Mg (~10^{-3} s^{-1}). The rates of dissolution range from 0.11 nm/hour to 0.47 nm/hour for SiO_2 with an initial thickness between 35 nm and 100 nm at a temperature between room and physiological temperatures. These rates of dissolution for PECVD SiO_2 in water are consistent with the rates reported in prior experiments (Wirth and Gieskes, 1979), which are higher than those for quartz (Worley, 1994).

In comparison to the intermittent thickness measurement, electrical properties can potentially provide continuous measurements. Electrical measurements also allow for evaluation of the dissolution behavior of a conductive material below a nonconductive layer, as discussed in the next section. The relative changes in both the width and length directions are much smaller than in the thickness direction. Therefore, the electric resistance is inversely proportional to the remaining thickness as $R = R_0 h_0/h \approx R_0/(1-t/t_c)$, where R_0 is the initial resistance. Changes of resistance approximately account for both changes in thickness and influences associated with porosity, pitting and other non-uniformities induced by non-uniform dissolution (Yin et al., 2014). The normalized electric resistance R/R_0 of Mg is shown in Figure 4c as a function of the normalized time t/t_c. In this figure, the same reaction constant k=1.2×10^{-3} s^{-1} and diffusivity D=6.0×10^{-12} cm^2/s are chosen for Mg with an initial thickness of 300 nm and initial resistance (per unit length) R_0 of 1.06 Ω/mm. It is important to note that an initial layer of thin MgO may exist on top of the Mg layer. In the presence of water, this thin MgO layer quickly reacts to form a more stable, crystalline hydroxide (Pourbaix, 1974), which is not as protective as non-crystalline films (Hoare, 1970). Thus, the single-layer dissolution model can properly account for the hydrolysis of Mg.

The potential of thin films made from other transient metals for use in transient electronics has also been explored and was found to be worth considering with the development of MOSFETs as an example (Yin et al., 2014). Analytical models discussed above are found to be

applicable to other dissolvable metals, including Mg alloy, zinc (Zn), tungsten (W), and molybdenum (Mo). The prediction from the model can reproduce the observed dissolution behaviors in deionized (DI) water and simulated body fluids (e.g., Hanks' solution with pH from 5 to 8) (Yin et al., 2014). Particularly, the electrical dissolution rates in thin films can be much different from traditionally reported corrosion rates in corresponding bulk materials. The model cannot, however, capture the dissolution behavior of iron (Fe), because Fe degrades in a spatially non-uniform manner, with certain reaction products (Fe_2O_3 and Fe_3O_4) that have very low solubility (Yin et al., 2014).

Silicon oxides and silicon nitrides are key materials for dielectrics and encapsulation layers in the class of silicon-based high performance electronics. The dissolution rates of these materials are affected by the physical and chemical properties of the films, which in turn depend on the deposition/growth methods and conditions. A key parameter that can approximately characterize these differences is density. The effects of density variation are two-fold. Reduced density increases the porosity in the porous materials, which results in an increased reactive surface to accelerate the dissolution. Secondly, it also reduces the amount of materials that need to be dissolved. The effective density ρ_{eff} of porous material is related to the density ρ_s of the fully dense materials as $\rho_{eff} = \rho_s V_s/(V_s + V_{air})$, where V_s and V_{air} are the volumes of the porous material and air cavity, respectively. A modified version of the reactive diffusion model provides a simple means to account for the density variation (Kang et al., 2014). In Equation (1), the diffusivity D is replaced with an effective diffusivity D_e. The effective diffusivity of water in a porous medium is linearly proportional to the pore fraction in the porous medium: $D_e \propto V_{air}/(V_{air} + V_s) = (\rho_s - \rho_{eff})/\rho_s$. As densities of porous materials from various deposition methods/conditions are measured directly from the experiment, the effective diffusivity of water in each porous material can be determined. At time t=0, the air pores are filled with water, i.e., $w|_{t=0} = w_0(\rho_s - \rho_{eff})/\rho_s \ (0 \le y < h_0)$. The boundary conditions remain the same as those for Equation (1). Following the same approach discussed above, the normalized thickness is solved as (Kang et al., 2014)

$$\frac{h}{h_0}=1-\frac{w_0 M}{q\rho_{eff} M_{H_2O}}\frac{kh_0^2}{D_e}\left\{\frac{D_e t}{h_0^2}\frac{\tanh\sqrt{\frac{kh_0^2}{D_e}}}{\sqrt{\frac{kh_0^2}{D_e}}}-2\sum_{n=1}^{\infty}C_n\frac{1-e^{-\left[\frac{kh_0^2}{D_e}+\left(n-\frac{1}{2}\right)^2\pi^2\right]\frac{D_e t}{h_0^2}}}{\left[\frac{kh_0^2}{D_e}+\left(n-\frac{1}{2}\right)^2\pi^2\right]}\right\}, \quad (6)$$

where C_n is $C_n=\left[kh_0^2/D_e+(n-1/2)^2\pi^2\right]^{-1}+\left(\rho_{eff}/\rho_s-1\right)/(n-1/2)^2\pi^2$. The dissolution rate is then estimated as $-dh/dt=kh_0\, w_0 M/\left(q\rho_{eff} M_{H_2O}\right)\tanh\sqrt{kh_0^2/D_e}/\sqrt{kh_0^2/D_e}$. With measured densities and calculated effective diffusivities, the reaction constants are found to be different for silicon oxides (or nitrides) deposited from different conditions as well. The results suggest that the density has affected the dissolution rate through changes in diffusion, as well as through differences in reactivity. Besides the dissolution at a molecular level, the removal of nanoscale pieces of material from the film may also be possible as narrow regions of the porous matrix disappear by hydrolysis. This discovery promises the future development of tunable dissoluion through geometrical variations. When combined with patterned structures in the transient materials or the encapsulation layer (to be discussed in the next section), the dissolution behavior of transient electronics may be tuned actively through changes of diffusivity and reactivity from deformation upon stimuli, including swelling, thermal and mechanical loadings.

Dissolution of the Device with Bi-layered Structures

Applications in biomedicine require the transient electronics to function stably in a certain timeframe, followed by a complete physical disappearance. All of the transient materials however, start to dissolve immediately in the bio-fluids. The lifetime of the resulting devices is typically determined by Mg interconnects due to their fast reaction with water. Although the system may function before it completely breaks down, its performance is significantly compromised. Therefore, it is important to explore a mechanism that allows devices to function in a programmed lifetime.

Adding encapsulation layers or packaging materials on top of the device can extend its lifetime in a controlled manner. For instance, MgO can serve as an encapsulation layer for Mg. In this bi-layered system (Figure 4b), zero initial condition at t=0 applies to both Mg and MgO

layers. The reactive diffusion Equation (1) together with zero water flux boundary condition at the bottom surface y=0 still holds for the Mg layer. As for the MgO encapsulation with an initial thickness of $h_{encapsulation}$, the reactive diffusion equation becomes (Li et al., 2013) $D_{\text{encapsulation}}\frac{\partial^2 w}{\partial y^2}-k_{\text{encapsulation}}w=\frac{\partial w}{\partial t}\ \left(h_0\le y\le h_0+h_{\text{encapsulation}}\right)$, where $D_{\text{encapsulation}}$ and $k_{\text{encapsulation}}$ are the diffusivity of water in MgO and reaction constant between MgO and water, respectively. The constant water concentration boundary condition at the MgO/water interface is $w\big|_{y=h_0+h_{\text{encapsulation}}}=w_0$. In addition, the continuity conditions of water concentration and flux across the MgO/Mg interface are $w\big|_{y=h_0-0}=w\big|_{y=h_0+0}$ and $D\partial w/\partial y\big|_{y=h_0-0}=D_{\text{encapsulation}}\,\partial w/\partial y\big|_{y=h_0+0}$. Similar to the single-layer system, the inhomogeneous boundary condition leads to a representation of the water concentration as a sum of a homogenous solution w_h and a particular solution w_p, i.e., w=w_h+w_p. The homogeneous solution w_h satisfies the homogeneous equation $D'\partial^2 w_h/\partial y^2-k'w_h=\partial w_h/\partial t$, where $D'=D$ and $k'=k$ for $0\le y\le h_0$ in the Mg layer, and $D'=D_{\text{encapsulation}}$ and $k'=k_{\text{encapsulation}}$ for $h_0\le y\le h_0+h_{\text{encapsulation}}$ in the MgO encapsulation. The boundary conditions become homogenous as well, i.e., $w_h\big|_{y=h_0+h_{\text{encapsulation}}}=0$, $\partial w_h/\partial y\big|_{y=0}=0$.

By the method of separation of variables, the homogenous solution is solved as $w_h=w_0\sum_{n=1}^{\infty}C_n e^{-\lambda_n t}f_n(y)$, where the coefficients C_n are to be determined from the initial condition, $\lambda_n\ (n=1,2,3,\ )$ can be solved from the following eigen equation

$$\tan\sqrt{\frac{\lambda-k}{D}}h_0\tan\sqrt{\frac{\lambda-k_{\text{encapsulation}}}{D_{\text{encapsulation}}}}h_{\text{encapsulation}}=\sqrt{\frac{\left(\lambda-k_{\text{encapsulation}}\right)D_{\text{encapsulation}}}{(\lambda-k)D}}, \tag{7}$$

and $f_n(y)$ is written as

$$f_n(y)\equiv\begin{cases}\sin\left(\sqrt{\dfrac{\lambda_n-k_{\text{encapsulation}}}{D_{\text{encapsulation}}}}h_{\text{encapsulation}}\right)\cos\left(\sqrt{\dfrac{\lambda_n-k}{D}}y\right), & 0\le y\le h_0\\ \cos\left(\sqrt{\dfrac{\lambda_n-k}{D}}h_0\right)\sin\left[\sqrt{\dfrac{\lambda_n-k_{\text{encapsulation}}}{D_{\text{encapsulation}}}}\left(h_0+h_{\text{encapsulation}}-y\right)\right], & h_0\le y\le h_0+h_{\text{encapsulation}}\end{cases}. \tag{8}$$

Satisfying the reactive diffusion equation, together with inhomogeneous boundary condition, zero water flux at the bottom of Mg layer, and continuity conditions, the particular solution w_p is solved as $w_p = w_0 g(y)$, where

$$g(y) \equiv \begin{cases} G\cosh\left(\sqrt{\dfrac{k}{D}}y\right), & 0 \le y \le h_0 \\ \cosh\left(\xi\dfrac{h_0 + h_{\text{encapsulation}} - y}{h_{\text{encapsulation}}}\right) - H\sinh\left(\xi\dfrac{h_0 + h_{\text{encapsulation}} - y}{h_{\text{encapsulation}}}\right), & h_0 \le y \le h_0 + h_{\text{encapsulation}} \end{cases}, \tag{9a, b}$$

$$G = \frac{1}{\sqrt{\dfrac{Dk}{D_{\text{encapsulation}}k_{\text{encapsulation}}}}\sinh\sqrt{\dfrac{kh_0^2}{D}}\sinh\xi + \cosh\sqrt{\dfrac{kh_0^2}{D}}\cosh\xi}$$

$$H = \frac{\sqrt{\dfrac{Dk}{D_{\text{encapsulation}}k_{\text{encapsulation}}}}\tanh\sqrt{\dfrac{kh_0^2}{D}} + \tanh\xi}{\sqrt{\dfrac{Dk}{D_{\text{encapsulation}}k_{\text{encapsulation}}}}\tanh\sqrt{\dfrac{kh_0^2}{D}}\tanh\xi + 1}, \tag{10a, b}$$

and $\xi = \sqrt{k_{\text{encapsulation}}h_{\text{encapsulation}}^2 / D_{\text{encapsulation}}}$. With the expression of the water concentration $w = w_0\left[\sum_{n=1}^{\infty} C_n e^{-\lambda_n t} f_n(y) + g(y)\right]$, the zero initial condition leads to $\sum_{n=1}^{\infty} C_n f_n(y) + g(y) = 0$. Orthogonality of eigenfunctions requires $\int_0^{h_0+h_{\text{encapsulation}}} f_m(y) f_n(y)\,dy = 0$ (if $m \neq n$), which yields the coefficient C_n analytically as

$$C_n = -\frac{\int_0^{h_0+h_{\text{encapsulation}}} f_n(y)\,g(y)\,dy = 0}{\int_0^{h_0+h_{\text{encapsulation}}} f_n^2(y)\,dy = 0}$$

$$= \frac{-\frac{2}{\lambda_n}\sqrt{\left(\lambda_n - k_{\text{encapsulation}}\right)D_{\text{encapsulation}}}\cos\left(\sqrt{\frac{\lambda_n - k}{D}}h_0\right)}{\left\{\begin{array}{l} h_0 \sin^2\left(\sqrt{\frac{\lambda_n - k_{\text{encapsulation}}}{D_{\text{encapsulation}}}}h_{\text{encapsulation}}\right)\left[1+\frac{\sin\left(2\sqrt{\frac{\lambda_n - k}{D}}h_0\right)}{2\sqrt{\frac{\lambda_n - k}{D}}h_0}\right] \\ +h_{\text{encapsulation}}\cos^2\left(\sqrt{\frac{\lambda_n - k}{D}}h_0\right)\left[1-\frac{\sin\left(2\sqrt{\frac{\lambda_n - k_{\text{encapsulation}}}{D_{\text{encapsulation}}}}h_{\text{encapsulation}}\right)}{2\sqrt{\frac{\lambda_n - k_{\text{encapsulation}}}{D_{\text{encapsulation}}}}h_{\text{encapsulation}}}\right] \end{array}\right\}}. \quad (11)$$

The expression given in Equation (11) completes the solution of the reactive diffusion equation for bi-layered structures. In addition to the dependence on y/h_0, Dt/h_0^2, and kh_0^2/D as in the single-layer solution, the normalized water concentration w/w_0 also depends on the normalized reaction constant $k_{\text{encapsulation}}h_{\text{encapsulation}}^2/D_{\text{encapsulation}}$ of the encapsulation layer, the diffusivity ratio $D_{\text{encapsulation}}/D$, and initial thickness ratio $h_{\text{encapsulation}}/h_0$. Because the diffusivity ratio $D_{\text{encapsulation}}/D$ is much smaller than 1, the water concentration in Mg is relatively uniform whereas that in MgO is not (Figure 3b). In comparison to Figure 3a, the water concentration in Mg increases much slower, which effectively extends the lifetime of Mg.

In the same manner as described in the previous section, the remaining thickness h of the Mg layer normalized by its initial thickness h_0 is obtained as

$$\frac{h}{h_0} = 1 - \frac{w_0 M}{q\rho M_{H_2O}}k\left[Gt\cdot\frac{\sinh\sqrt{\frac{kh_0^2}{D}}}{\sqrt{\frac{kh_0^2}{D}}} + \sum_{n=1}^{\infty}\frac{C_n}{\lambda_n}\left(1-e^{-\lambda_n t}\right)\frac{\sin\sqrt{\frac{\lambda_n - k}{D}h_0^2}}{\sqrt{\frac{\lambda_n - k}{D}h_0^2}}\sin\sqrt{\frac{\lambda_n - k_{\text{encapsulation}}}{D_{\text{encapsulation}}}h_{\text{encapsulation}}^2}\right], \quad (12)$$

where G is given in Equation (10a). As Mg is below the MgO encapsulation layer, it is difficult to measure the thickness change of Mg. Noticing MgO is not conductive, the electric resistance

of Mg (or this bi-layered structure) is then measured, from which the thickness can be calculated $h = R_0 h_0 / R$. To understand the thickness effect of MgO encapsulation, both 400 nm-thick and 800 nm-thick MgO layers are studied on a 300nm-thick Mg layer. As shown in Figure 4c, the normalized electrical resistance R/R_0 versus the normalized time Dt/h_0^2 predicted from the theory agrees well with the experimental measurements. A comparison between two Mg + MgO structure layouts indicates a substantial increase in the dissolution time as the thickness of encapsulation layer increases. This comes from the fact that the diffusion of water in MgO is much slower than that in Mg, which effectively extends the lifetime of Mg in providing an effective way to control the dissolution time.

The summation on the right hand side of Equation (12) is negligible for devices relevant to transient implants. As a result, the thickness decreases linearly with time. The simple and approximate expression is given as $h/h_0 \approx 1 - t/t_c'$, where

$$t_c' = \frac{t_c}{G\cosh\sqrt{\frac{kh_0^2}{D}}} = t_c\left(\sqrt{\frac{kD}{k_{\text{encapsulation}}D_{\text{encapsulation}}}}\tanh\sqrt{\frac{kh_0^2}{D}}\sinh\xi + \cosh\xi\right) \tag{13}$$

is the critical time for complete physical disappearance of the Mg conductor layer in the device and t_c is the critical time in the single-layer system. From the remaining thickness h, the rate of dissolution can be solved as $v_{\text{dissolution}} = -dh/dt \approx h_0/t_c'$. The rate of dissolution is approximately linear with the initial thickness h_0 and it can be further simplified for a sufficiently thin Mg layer ($kh_0^2/D << 1$) as $v_{\text{dissolution}} = w_0 M / \left(q\rho M_{H_2O}\right)\left(kh_0/\cosh\xi\right)$.

As an alternative, silicon oxides and nitrides can also be considered as encapsulation layers in addition to their use as gate and interlayer dielectrics, as they are typically known to be barrier materials for permeation of water (Kang et al., 2014). As a primary source of leakage for vapors or fluids, defects such as pinholes are commonly found in films of silicon oxides and nitrides. As a result, multilayer structures with different materials (Kang et al., 2014) have been developed to cooperatively eliminate defects (Rosink et al., 2005) for use in transient electronics. In addition to a combination of multiple different layers, i.e. SiO_2 and Si_3N_4 (Figure 5a left), atomic layer deposition (ALD) provides a complementary strategy to reduce defects and improve the performance of the encapsulation, even with thin layers (Figure 5a, right) (Meyer et al., 2009). As shown in Figure 5b, measured changes in resistance of a serpentine-shaped Mg trace

with an initial thickness of 300 nm demonstrate the effectiveness of several encapsulation approaches.

To achieve an even longer desired lifetime for transient electronic devices, silk overcoats have also been used to provide an extra barrier for water to diffuse into MgO and Mg layers (Hwang et al., 2012). A well designed layout with both MgO encapsulation and silk overcoat can successfully increase the lifetime of devices over hundreds of times (Li et al., 2013). To apply the idea of multilayer structures to silk overcoats, an encapsulation strategy of exploiting multiple air pockets has been demonstrated (Brenckle et al., 2015). A scheme of this strategy is shown in Figure 5c. Transient electronics transferred to a silk substrate are enclosed by silk films with tunable crystalline and diffusion properties. Thermal sealing of the silk films creates a small air pocket, which provides additional protection for the device components. Iteration of this process can provide multiple silk pockets as needed. The onset of device degradation starts only when swelling of the silk protective layer collapses the air pocket in a wet environment (Lawrence et al., 2010).

These combined strategies in encapsulation lead to two-stage dissolution kinetics in transient electronics: i) encapsulation layers define the first time period of stable operation with negligible changes in electrical performance, ii) the Mg defines the second, where the device rapidly degrades. Efficient encapsulation strategies can remove the leakage pathways and significantly increase the time for stable operation. Realizing the full potential of transient electronics for implanted applications ultimately requires conformal contact with organs of the body. To this end, a recent development of transient medical devices exploits the concepts of stretchable electronics (Cheng et al., 2014; Cheng et al., 2011; Kim et al., 2011a; Rogers et al., 2010; Viventi et al., 2010) by use of biodegradable elastomers (Hwang et al., 2015a). As shown in optical images and schematic illustrations (Figures 6a and b), a stretchable and transient electrophysiology sensor is constructed. Thin layers of Mg (300 nm) and SiO_2 (100 nm) are designed in the form of filamentary serpentine meshes (Kim et al., 2010; Kim et al., 2008; Kim et al., 2011b) (Figure 6a, inset) for measurement, ground and reference electrodes and connecting leads. Capacitive sensing leads to the use of a biodegradable polymer (Hwang et al., 2014c; Yang et al., 2004) between the Mg electrodes and the skin. The measurements show levels of fidelity comparable to those of conventional gel electrodes (Figure 6d), as demonstrated in the high quality electrocardiograms (ECG) measurements on the chest (Figure 6c). Figure 6e presents a set of

images of a transient electrophysiology sensor at various dissolution stages in PBS (pH 10) at room temperature. The dissolution behavior of each component is consistent with separate studies of these materials discussed in the previous section (complete dissolution within hours for Mg or days/weeks for SiO_2).

Conclusion

When exposed to bio-fluids or water, the class of silicon-based high performance transient electronics disintegrates and dissolves to eliminate the need for recollection. A number of discoveries have been made in the effort to control how transient electronics dissolve. Firstly, a number of materials, including semiconductors, and their method of application in the design of transient electronics were studied. Secondly, a model of reactive diffusion was presented to predict the way in which a component would dissolve in bio-fluids or water. This model considered a variety of factors including the porosity of the material. Thirdly, this model was extended to study the reactive diffusion in a bi-layered structure. The analytical results connect the key electrical property to models of reactive diffusion and provide the capability to use such analytics in conjunction with established circuit simulators as a comprehensive design approach.

Since the nature of the materials used in transient electronics exhibit a decisive effect on the dissolution of resulting electronics, future material science research would be desirable. Other strategies besides encapsulation would also be worth future research to understand multiple ways of controlling the dissolution behavior of transient electronics. Active control of the transience in devices is of interest for the future development as well. Combining possibilities in transient electronics with ideas in soft, "tissue-like" devices further expands opportunities for applications in biomedicine. Overall, however, the research performed thus far on the design of transient electronics has been extensive and the potential use of this technology in industry is evident.

Acknowledgements

H. C. was a Howard Hughes Medical Institute International Student Research fellow. The authors acknowledge the start-up fund provided by the Engineering Science and Mechanics De-

partment, College of Engineering, and Materials Research Institute at The Pennsylvania State University.

References

Bettinger, C.J., and Bao, Z. (2010). Organic Thin-Film Transistors Fabricated on Resorbable Biomaterial Substrates. Adv Mater *22*, 651-655.

Brenckle, M.A., Cheng, H., Hwang, S., Tao, H., Paquette, M., Kaplan, D.L., Rogers, J.A., Huang, Y., and Omenetto, F.G. (2015). Modulated degradation of transient electronic devices through multilayer silk fibroin pockets. ACS applied materials & interfaces.

Cheng, H., Zhang, Y., Hwang, K.-C., Rogers, J.A., and Huang, Y. (2014). Buckling of a stiff thin film on a pre-strained bi-layer substrate. International Journal of Solids and Structures *51*, 3113-3118.

Cheng, H., Wu, J., Li, M., Kim, D.H., Kim, Y.S., Huang, Y., Kang, Z., Hwang, K.C., and Rogers, J.A. (2011). An analytical model of strain isolation for stretchable and flexible electronics. Applied Physics Letters *98*, 061902.

Dagdeviren, C., Hwang, S.W., Su, Y., Kim, S., Cheng, H., Gur, O., Haney, R., Omenetto, F.G., Huang, Y., and Rogers, J.A. (2013). Transient, Biocompatible Electronics and Energy Harvesters Based on ZnO. Small.

Danckwerts, P.V. (1950). Absorption by simultaneous diffusion and chemical reaction. Transactions of the Faraday Society *46*, 300.

Darouiche, R.O. (2004). Treatment of infections associated with surgical implants. New England Journal of Medicine *350*, 1422-1429.

Eder, F., Klauk, H., Halik, M., Zschieschang, U., Schmid, G., and Dehm, C. (2004). Organic electronics on paper. Applied Physics Letters *84*, 2673-2675.

Hernandez, H.L., Kang, S.K., Lee, O.P., Hwang, S.W., Kaitz, J.A., Inci, B., Park, C.W., Chung, S., Sottos, N.R., and Moore, J.S. (2014). Triggered Transience of Metastable Poly (phthalaldehyde) for Transient Electronics. Adv Mater *26*, 7637-7642.

Hoare, J.P. (1970). Oxide film studies on iron in electrochemical machining electrolytes. J Electrochem Soc *117*, 142-145.

Huang, X., Liu, Y., Hwang, S.W., Kang, S.K., Patnaik, D., Cortes, J.F., and Rogers, J.A. (2014). Biodegradable Materials for Multilayer Transient Printed Circuit Boards. Adv Mater *26*, 7371-7377.

Hwang, S.-W., Park, G., Edwards, C., Corbin, E.A., Kang, S.-K., Cheng, H., Song, J.-K., Kim, J.-H., Yu, S., and Ng, J. (2014a). Dissolution Chemistry and Biocompatibility of Single-Crystalline Silicon Nanomembranes and Associated Materials for Transient Electronics. Acs Nano *8*, 5843-5851.

Hwang, S.-W., Lee, C.H., Cheng, H., Jeong, J.-W., Kang, S.-K., Kim, J.-H., Shin, J., Yang, J., Liu, Z., and Ameer, G.A. (2015a). Biodegradable Elastomers and Silicon Nanomembranes/Nanoribbons for Stretchable, Transient Electronics, and Biosensors. Nano Letters *15*, 2801-2808.

Hwang, S.-W., Tao, H., Kim, D.-H., Cheng, H., Song, J.-K., Rill, E., Brenckle, M.A., Panilaitis, B., Won, S.M., Kim, Y.-S., Song, Y.M., Yu, K.J., Ameen, A., Li, R., Su, Y., Yang, M., Kaplan, D.L., Zakin, M.R., Slepian, M.J., Huang, Y., Omenetto, F.G., and Rogers, J.A. (2012). A Physically Transient Form of Silicon Electronics. Science *337*, 1640-1644.

Hwang, S.W., Kang, S.K., Huang, X., Brenckle, M.A., Omenetto, F.G., and Rogers, J. (2015b). Materials for Programmed, Functional Transformation in Transient Electronic Systems. Adv Mater *27*, 47-52.

Hwang, S.W., Park, G., Cheng, H., Song, J.K., Kang, S.K., Yin, L., Kim, J.H., Omenetto, F.G., Huang, Y., and Lee, K.M. (2014b). 25th Anniversary Article: Materials for High-Performance Biodegradable Semiconductor Devices. Adv Mater *26*, 1992-2000.

Hwang, S.W., Song, J.K., Huang, X., Cheng, H., Kang, S.K., Kim, B.H., Kim, J.H., Yu, S., Huang, Y., and Rogers, J.A. (2014c). High-Performance Biodegradable/Transient Electronics on Biodegradable Polymers. Adv Mater *26*, 3905-3911.

Inoue, H., Sugahara, K., Yamamoto, A., and Tsubakino, H. (2002). Corrosion rate of magnesium and its alloys in buffered chloride solutions. Corrosion Science *44*, 603-610.

Irimia-Vladu, M., Troshin, P.A., Reisinger, M., Shmygleva, L., Kanbur, Y., Schwabegger, G., Bodea, M., Schwödiauer, R., Mumyatov, A., and Fergus, J.W. (2010). Biocompatible and Biodegradable Materials for Organic Field-Effect Transistors. Advanced Functional Materials *20*, 4069-4076.

Kang, S.-K., Park, G., Kim, K., Hwang, S.-W., Cheng, H., Shin, J., Chung, S., Kim, M., Yin, L., and Lee, J.C. (2015). Dissolution Chemistry and Biocompatibility of Silicon-and Germanium-Based Semiconductors for Transient Electronics. ACS applied materials & interfaces *7*, 9297-9305.

Kang, S.K., Hwang, S.W., Cheng, H., Yu, S., Kim, B.H., Kim, J.H., Huang, Y., and Rogers, J.A. (2014). Dissolution Behaviors and Applications of Silicon Oxides and Nitrides in Transient Electronics. Advanced Functional Materials *24*, 4427-4434.

Kim, D.-H., Lu, N., Ma, R., Kim, Y.-S., Kim, R.-H., Wang, S., Wu, J., Won, S.M., Tao, H., Islam, A., Yu, K.J., Kim, T.-i., Chowdhury, R., Ying, M., Xu, L., Li, M., Chung, H.-J., Keum, H., McCormick, M., Liu, P., Zhang, Y.-W., Omenetto, F.G., Huang, Y., Coleman, T., and Rogers, J.A. (2011a). Epidermal Electronics. Science *333*, 838-843.

Kim, D.H., Xiao, J.L., Song, J.Z., Huang, Y.G., and Rogers, J.A. (2010). Stretchable, Curvilinear Electronics Based on Inorganic Materials. Adv Mater *22*, 2108-2124.

Kim, D.H., Kim, Y.S., Amsden, J., Panilaitis, B., Kaplan, D.L., Omenetto, F.G., Zakin, M.R., and Rogers, J.A. (2009). Silicon electronics on silk as a path to bioresorbable, implantable devices (vol 95, 133701, 2009). Applied Physics Letters *95*.

Kim, D.H., Ahn, J.H., Choi, W.M., Kim, H.S., Kim, T.H., Song, J.Z., Huang, Y.G.Y., Liu, Z.J., Lu, C., and Rogers, J.A. (2008). Stretchable and foldable silicon integrated circuits. Science *320*, 507-511.

Kim, R.H., Bae, M.H., Kim, D.G., Cheng, H., Kim, B.H., Kim, D.H., Li, M., Wu, J., Du, F., Kim, H.S., Kim, S., Estrada, D., Hong, S.W., Huang, Y., Pop, E., and Rogers, J. (2011b). Stretchable, Transparent Graphene Interconnects for Arrays of Microscale Inorganic Light Emitting Diodes on Rubber Substrates. Nano Letters *11*, 3381-3886.

Lawrence, B.D., Wharram, S., Kluge, J.A., Leisk, G.G., Omenetto, F.G., Rosenblatt, M.I., and Kaplan, D.L. (2010). Effect of hydration on silk film material properties. Macromolecular bioscience *10*, 393-403.

Lee, C.H., Kang, S.K., Salvatore, G.A., Ma, Y., Kim, B.H., Jiang, Y., Kim, J.S., Yan, L., Wie, D.S., and Banks, A. (2015). Wireless Microfluidic Systems for Programmed, Functional Transformation of Transient Electronic Devices. Advanced Functional Materials *25*, 5100-5106.

Li, R., Cheng, H., Su, Y., Hwang, S.-W., Yin, L., Tao, H., Brenckle, M.A., Kim, D.-H., Omenetto, F.G., Rogers, J.A., and Huang, Y. (2013). An Analytical Model of Reactive Diffusion for Transient Electronics. Advanced Functional Materials *23*, 3106-3114.

Meyer, J., Görrn, P., Bertram, F., Hamwi, S., Winkler, T., Johannes, H.H., Weimann, T., Hinze, P., Riedl, T., and Kowalsky, W. (2009). Al2O3/ZrO2 Nanolaminates as Ultrahigh Gas-Diffusion Barriers—A Strategy for Reliable Encapsulation of Organic Electronics. Adv Mater *21*, 1845-1849.

Ng, W., Chiu, K., and Cheng, F. (2010). Effect of pH on the< i> in vitro</i> corrosion rate of magnesium degradable implant material. Materials Science and Engineering: C *30*, 898-903.

Park, C.W., Kang, S.K., Hernandez, H.L., Kaitz, J.A., Wie, D.S., Shin, J., Lee, O.P., Sottos, N.R., Moore, J.S., and Rogers, J.A. (2015). Thermally Triggered Degradation of Transient Electronic Devices. Adv Mater.

Pourbaix, M. (1974). Atlas of electrochemical equilibria in aqueous solutions.

Rimstidt, J.D., and Barnes, H.L. (1980). The Kinetics of Silica-Water Reactions. Geochim Cosmochim Ac *44*, 1683-1699.

Rogers, J.A., Someya, T., and Huang, Y.G. (2010). Materials and mechanics for stretchable electronics. Science *327*, 1603-1607.

Rosink, J., Lifka, H., Rietjens, G., and Pierik, A. (2005). 34.1: Ultra-Thin Encapsulation for Large-Area OLED Displays. Paper presented at: SID Symposium Digest of Technical Papers (Wiley Online Library).

Seidel, H., Csepregi, L., Heuberger, A., and Baumgartel, H. (1990a). Anisotropic Etching of Crystalline Silicon in Alkaline-Solutions .2. Influence of Dopants. J Electrochem Soc *137*, 3626-3632.

Seidel, H., Csepregi, L., Heuberger, A., and Baumgartel, H. (1990b). Anisotropic Etching of Crystalline Silicon in Alkaline-Solutions .1. Orientation Dependence and Behavior of Passivation Layers. J Electrochem Soc *137*, 3612-3626.

Tao, H., Hwang, S.-W., Marelli, B., An, B., Moreau, J.E., Yang, M., Brenckle, M.A., Kim, S., Kaplan, D.L., and Rogers, J.A. (2014). Silk-based resorbable electronic devices for remotely controlled therapy and in vivo infection abatement. Proceedings of the National Academy of Sciences *111*, 17385-17389.

Taub, I.A., Roberts, W., LaGambina, S., and Kustin, K. (2002). Mechanism of Dihydrogen Formation in the Magnesium-Water Reaction⊥. The Journal of Physical Chemistry A *106*, 8070-8078.

Viventi, J., Kim, D.H., Moss, J.D., Kim, Y.S., Blanco, J.A., Annetta, N., Hicks, A., Xiao, J.L., Huang, Y.G., Callans, D.J., Rogers, J.A., and Litt, B. (2010). A Conformal, Bio-Interfaced Class of Silicon Electronics for Mapping Cardiac Electrophysiology. Science Translational Medicine *2*.

Wirth, G., and Gieskes, J. (1979). The initial kinetics of the dissolution of vitreous silica in aqueous media. Journal of Colloid and Interface Science *68*, 492-500.

Worley, W.G. (1994). Dissolution kinetics and mechanisms in quartz-and grainite-water systems (Massachusetts Institute of Technology).

Yang, J., Webb, A.R., and Ameer, G.A. (2004). Novel Citric Acid-Based Biodegradable Elastomers for Tissue Engineering. Adv Mater *16*, 511-516.

Yin, L., Farimani, A.B., Min, K., Vishal, N., Lam, J., Lee, Y.K., Aluru, N.R., and Rogers, J.A. (2015). Mechanisms for Hydrolysis of Silicon Nanomembranes as Used in Bioresorbable Electronics. Adv Mater *27*, 1857-1864.

Yin, L., Cheng, H., Mao, S., Haasch, R., Liu, Y., Xie, X., Hwang, S.W., Jain, H., Kang, S.K., and Su, Y. (2014). Dissolvable Metals for Transient Electronics. Advanced Functional Materials *24*, 645-658.

Figure Captions

Figure 1. Proof-of-concept demonstration for transient electronics, with key materials and device structure layout. (a) Image of a device with all components deployed on a thin silk substrate. The device components include transistors, diodes, inductors, capacitors, and resistors, with interconnects and interlayer dielectrics. (b) Schematic illustration in an exploded view, with a top view in the lower right inset. (c) Images showing the time sequence at various dissolution stages in deionized (DI) water. Reprinted with permission from (Hwang et al., 2012)

Figure 2. Experiments of silicon dissolution with corresponding theoretical and numerical analyses. (a) Atomic force microscope topographical images of a silicon nanomembrane (Si NM) with initial dimension of 3 μm × 3 μm × 70 nm at various stages of hydrolysis in PBS at 37°C. Reprinted with permission from (Hwang et al., 2012) (b) Theoretical (lines) and experimental (symbols) dissolution of Si NMs from (a) in buffer solutions at different pH levels (pH 6, black; pH 7, red; pH 8, blue; pH 10, purple), at physiological temperature (37 ^{o}C). Reprinted with permission from (Hwang et al., 2014b). (c) Atomic configurations for each ion adsorption event in DFT simulation of the silicon dissolution process. Reprinted with permission from (Yin et al., 2015)

Figure 3. Distribution of water concentration predicted from models of reactive diffusion for the normalized time Dt/h_0^2 =0.1, 0.2, 0.4, 0.8, 2 and ∞ in (a) an Mg layer (kh_0^2/D=0.18) without encapsulation layer, and (b) both an Mg conductor layer encapsulated by an MgO layer (kh_0^2/D=0.18, $D_{\text{encapsulation}}/D$=0.082, $h_{\text{encapsulation}}/h_0$ =1.3, and $k_{\text{encapsulation}}h_{\text{encapsulation}}^2/D_{\text{encapsulation}}$ =1.6). Reprinted with permission from (Li et al., 2013)

Figure 4. Schematic illustrations for models of reactive diffusion and modeling predictions of the electrical resistance compared with experimental measurements. a) Single-layered structure and b) bi-layered structure used in models of reactive diffusion for porous materials. (c) Experimental and modeling results of the electric resistance of Mg and Mg with different en-

capsulation strategies (e.g. MgO encapsulation layers and/or silk overcoats). Reprinted with permission from (Li et al., 2013)

Figure 5. Encapsulation strategies with multilayer structures. (a) Schematic illustrations of encapsulation methods for transient electronic devices, with defects (e.g. pinholes) covered by a bilayer of SiO_2/Si_3N_4 (left) or an ALD layer (right). (b) Measurements of changes in resistance of Mg traces with an initial thickness of 300 nm encapsulated with different encapsulation approaches (in deionized water at room temperature). Encapsulation strategies examined here include a single layer of PECVD SiO_2 (black, 1 μm), PECVD-LF Si_3N_4 (red, 1 μm) and ALD SiO_2 (orange, 20 nm); a double layer of PECVD SiO_2/PECVD-LF Si_3N_4 (blue, 500/500 nm), PECVD SiO_2/ALD SiO_2 (magenta, 500/20 nm), PECVD-LF Si_3N_4/ALD SiO_2 (purple, 500/20 nm); and a triple layer of PECVD SiO_2/PECVD-LF Si_3N_4 (Cyan, 200/200/200/200/100/100 nm). Reprinted with permission from (Kang et al., 2014) (c) Fabrication strategy for the multilayer silk pocket. Crystallization of the outer layers renders them water insoluble, whereas the inner device substrate layer can remain crystallized. Sealing the outer edges around the device encapsulates it in a protective silk pocket. Multilayer fabrication is carried out by repeating the process with an inner pocket as the device layer. Reprinted with permission from (Brenckle et al., 2015)

Figure 6. Transient electrophysiological sensors configured in a stretchable pattern for capacitive sensing. (a) Optical image of a device and (inset) magnified view of electrode structures in the filamentary serpentine mesh layout. (b) Schematic illustration in an exploded view for the corresponding device in (a). (c) Photograph of a device mounted on the chest for measurement of electrocardiograms (ECG). (d) ECG measurements collected from transient (red) and standard gel-based (blue) devices. (e) A series of images at various dissolution stages of a transient device in PBS (pH 10) at room temperature. Reprinted with permission from (Hwang et al., 2015a)

Figure

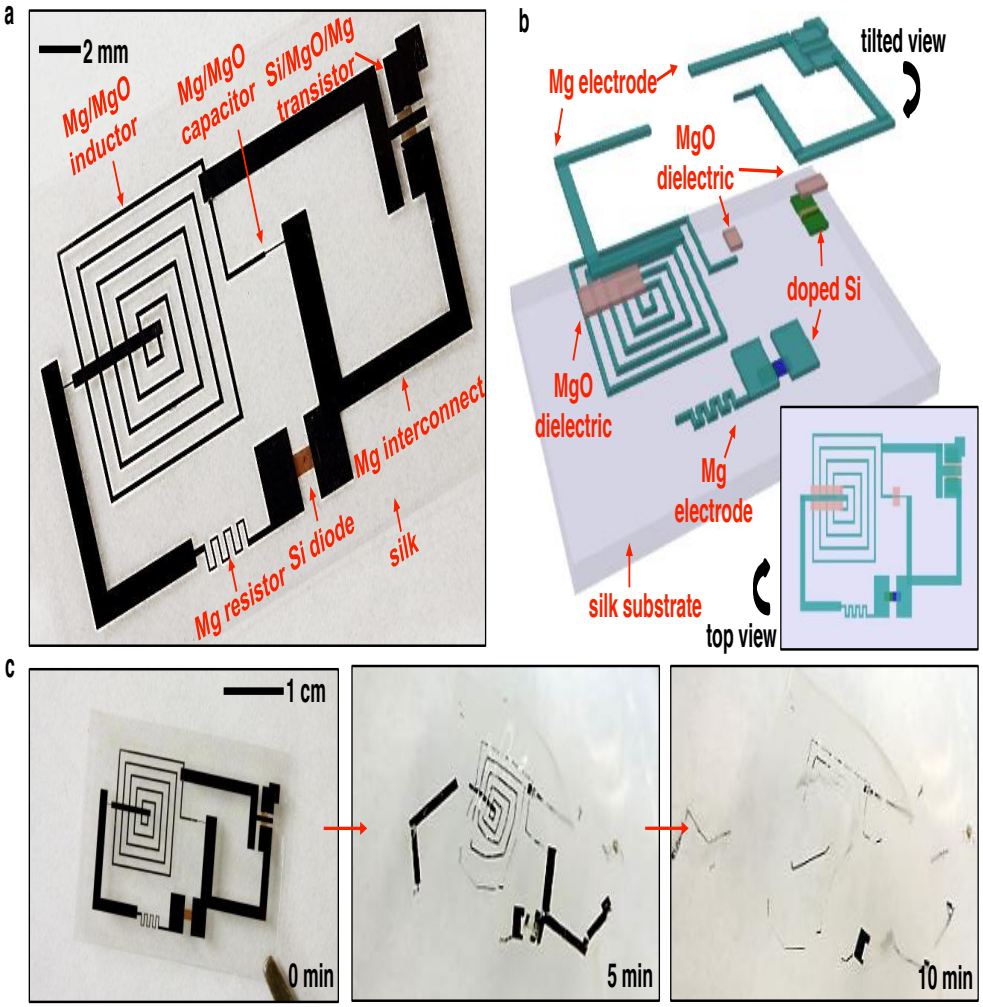

Figure 1

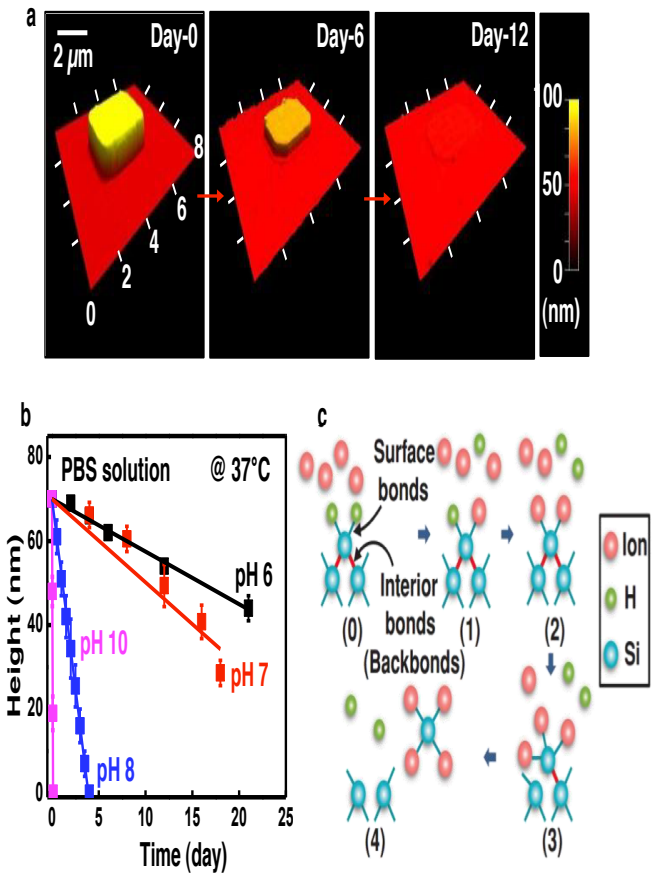
a
2 μm
Day-0
Day-6
Day-12
8
6
4
2
0
00
50
0
(nm)
b
PBS solution
@ 37°C
pH 6
pH 7
pH 10
pH 8
Height (nm)
Time (day)
c
Surface bonds
Interior bonds
(Backbonds)
(0)
(1)
(2)
(3)
(4)
Ion
H
Si

Figure 2

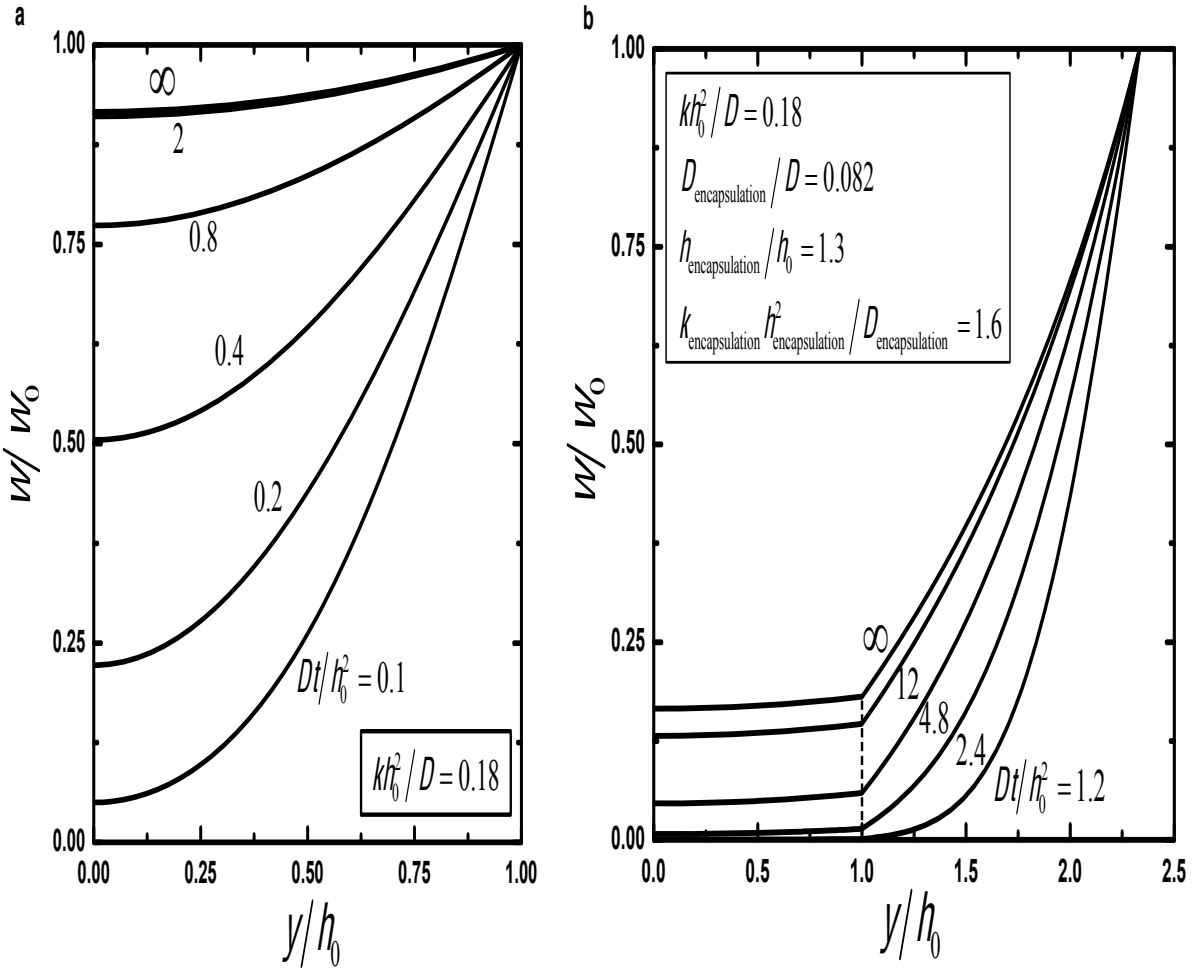
a
1.00
0.75
0.50
0.25
0.00
0.00
0.25
0.50
0.75
1.00
∞
2
0.8
0.4
0.2
$Dt/h_0^2 = 0.1$
$kh_0^2/D = 0.18$
w/w_0
y/h_0
b
$kh_0^2/D = 0.18$
$D_{encapsulation}/D = 0.082$
$h_{encapsulation}/h_0 = 1.3$
$k_{encapsulation}h^2_{encapsulation}/D_{encapsulation} = 1.6$
∞
12
4.8
2.4
$Dt/h_0^2 = 1.2$
0.0
0.5
1.0
1.5
2.0
2.5

Figure 3

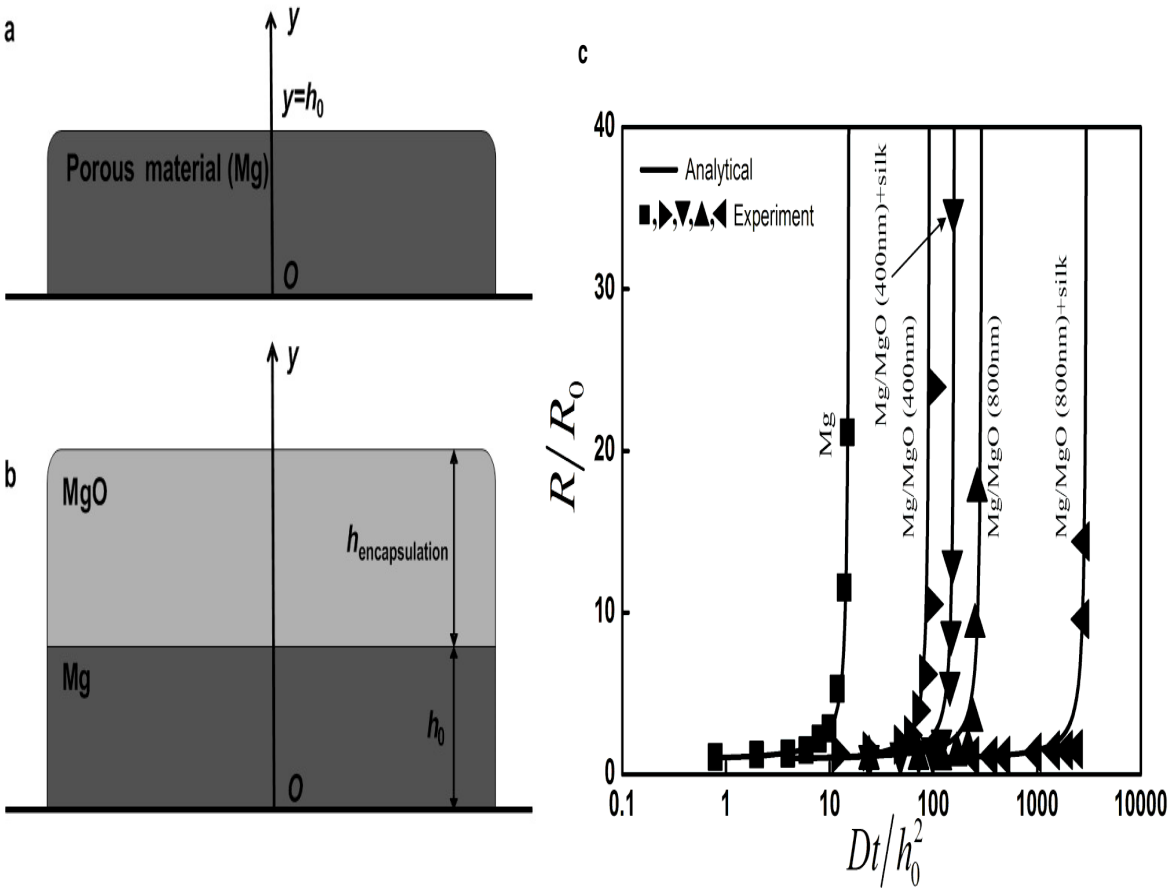
a
y
y=h0
Porous material (Mg)
O
b
y
MgO
hencapsulation
Mg
h0
O
c
Analytical
■,▶,▼,▲,◀ Experiment
Mg
Mg/MgO (400nm)+silk
Mg/MgO (400nm)
Mg/MgO (800nm)
Mg/MgO (800nm)+silk
R/R0
Dt/h0^2
0
10
20
30
40
0.1
1
10
100
1000
10000

Figure 4

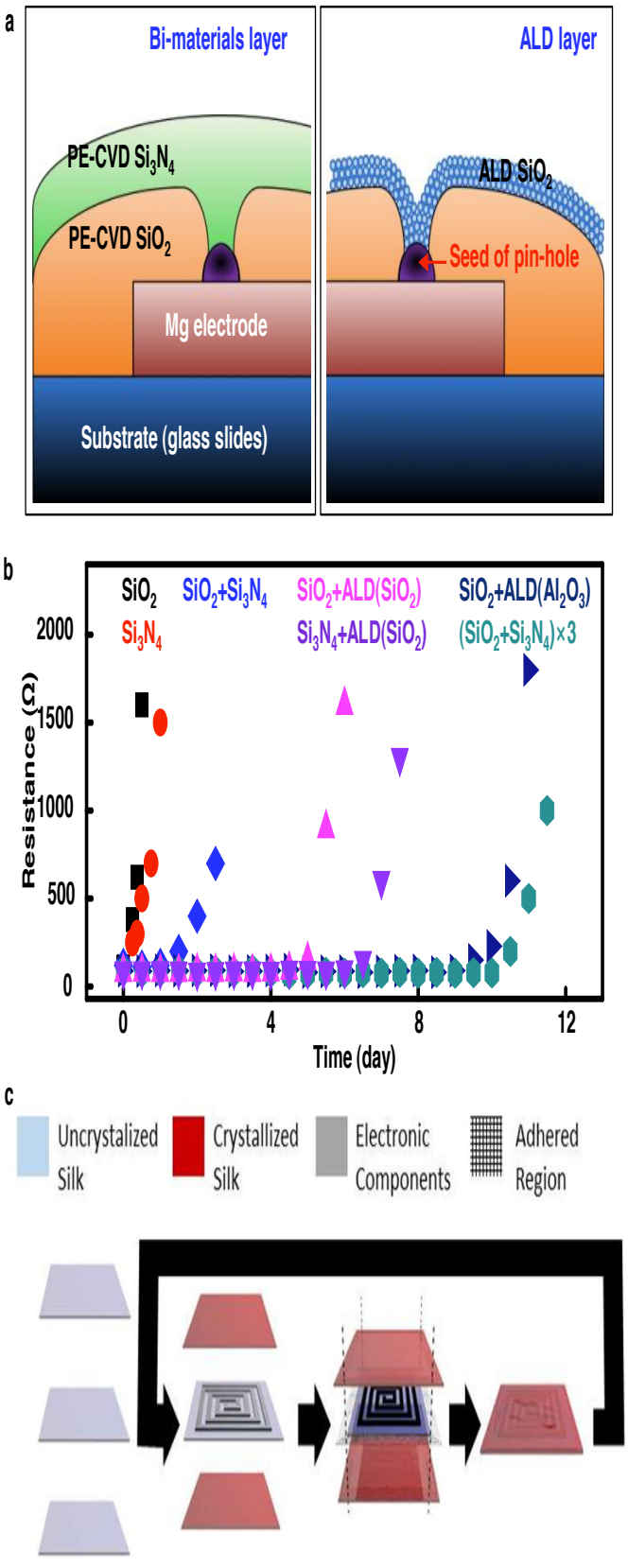
a
Bi-materials layer
ALD layer
PE-CVD Si_3N_4
PE-CVD SiO_2
Mg electrode
Substrate (glass slides)
ALD SiO_2
Seed of pin-hole
b
SiO_2
SiO_2+Si_3N_4
SiO_2+ALD(SiO_2)
SiO_2+ALD(Al_2O_3)
Si_3N_4
Si_3N_4+ALD(SiO_2)
(SiO_2+Si_3N_4)×3
Resistance (Ω)
2000
1500
1000
500
0
0
4
8
12
Time (day)
c
Uncrystalized Silk
Crystallized Silk
Electronic Components
Adhered Region

Figure 5

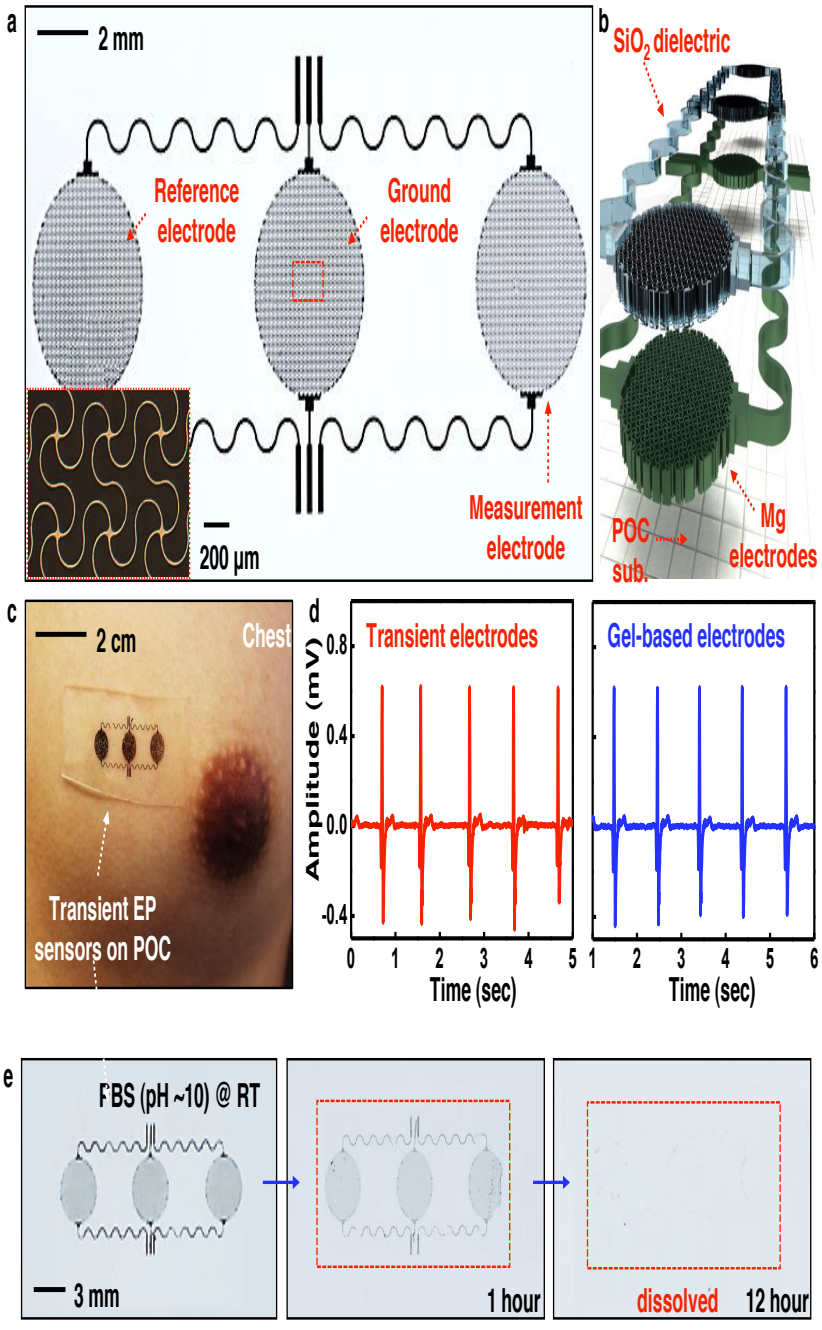
a
2 mm
Reference electrode
Ground electrode
Measurement electrode
200 μm
b
SiO2 dielectric
POC sub.
Mg electrodes
c
2 cm
Chest
Transient EP sensors on POC
d
Transient electrodes
Gel-based electrodes
Amplitude (mV)
0.8
0.4
0.0
-0.4
0 1 2 3 4 5
Time (sec)
1 2 3 4 5 6
Time (sec)
e
PBS (pH ~10) @ RT
3 mm
1 hour
dissolved
12 hour

Figure 6